Resilience-oriented Transmission Expansion Planning under Hurricane Impact Considering Vulnerable Line Identification and Hardening

Jing Zhou, Heng Zhang, Haozhong Cheng, Shenxi Zhang, Zheng Wang, and Xiaohu Zhang

***Abstract*—Resilient enhancement measures are crucial for increasing systems' capacities to deal with extreme natural disasters. However, in the pre-disaster prevention stage of hurricanes, research that simultaneously considers load importance, vulnerable lines, and multiple resilience enhancement measures is lacking. To address this issue, a novel resilience-oriented transmission expansion planning (ROTEP) model is proposed that incorporates two resilience assessment indices: the combined loss of loads (CLL) and the vulnerable line survival proportion (VLSP). In addition, the novel function of the proposed model meets the requirements of normal and hurricane damage scenarios based on the collaborative implementation of three resilience enhancement measures (expansion planning, hardening, and unit commitment). The proposed ROTEP model is structured in two stages. The first-stage model aims to meet the load growth demand while minimizing the total planning cost of transmission lines, the operating cost of generators, and the penalty cost of wind power and load shedding across several normal scenarios. Based on the scheme obtained from the first-stage model, damage scenarios are constructed, and a fault chain set is formulated using a hurricane simulation model. Then, a cascading fault graph is constructed to identify vulnerable lines. The second-stage model further enhances the CLL and VLSP (if necessary) under several damage scenarios by hardening the highest-contributing or most vulnerable line. Finally, the efficacy of the proposed ROTEP model for enhancing resilience is validated with a modified IEEE RTS-24 system and a two-area IEEE RTS-1996 system.**

***Index Terms*—Vulnerable line identification, resilience enhancement measures, hardening, unit commitment, transmission expansion planning.**

I. Introduction

The rising frequency and severity of natural disasters, exacerbated by climate change, significantly threaten the reliability of power systems, leading to significant economic losses [1]. For example, Hurricane Sandy in 2012 resulted in $50 billion losses in the United States. In 2016, hurricane Hermine caused $71.4 billion losses and resulted in power outages affecting 8.5 million users [2]. Weather-induced power outages are estimated to result in an average annual loss of $60 billion in the United States [3]. These issues highlight the critical need to implement adaptation measures to address the risk of power system disruptions caused by extreme natural disasters. The limitations of reliability criteria for identifying events with high impact and low probability have prompted a global focus on enhancing power system resilience [4]–[6].

Resilience, defined by the ability to anticipate, adapt to, and swiftly recover from disruptive events, is crucial for reinforcing power systems' capacities to withstand and respond to unforeseen extreme events [7]. In [8], resilience enhancement measures for power systems are classified into two primary categories: preventive and restorative. Several studies in [9]–[19] have examined the effectiveness of the implementation of individual preventive measures (namely, planning, hardening, and preventive response) in the pre-event stage to increase system resilience during disasters.

References [9]–[11] explore the enhancement of system resilience through the implementation of hardening measures (HMs). These measures can change the physical characteristics of infrastructure components and their surrounding environment, and subsequently, components can be upgraded with more robust materials, and overhead lines can be grounded. In [9], the load loss (LL) during extreme weather events is utilized as a resilience assessment index (RAI), and this index is then minimized through the implementation of HMs. Reference [10] explore the synergistic impact of HMs and optimally design microgrids to enhance system resilience. This approach is based on LL and the number of

Received: May 16, 2024
Accepted: August 21, 2024
Published Online: May 1, 2025
Jing Zhou, Heng Zhang (corresponding author), Haozhong Cheng, and Shenxi Zhang are with the Key Laboratory of Control of Power Transmission and Conversion, Ministry of Education, Electrical Engineering Department, Shanghai Jiao Tong University, Shanghai 200240, China (e-mail: zhou_j@sjtu.edu.cn; zhangheng_sjtu@sjtu.edu.cn; cheng_haozhong@163.com; 1527835143@qq.com).
Zheng Wang and Xiaohu Zhang are with the East China Branch of State Grid Corporation, Shanghai 200120, China (e-mail: 755705814@qq.com; 517706660@qq.com).
DOI: 10.23919/PCMP.2024.000063

disrupted components, according to their RAIs. In [11], a hardening strategy is devised for multiple concurrent extreme natural disaster scenarios, aiming to minimize the expected load loss (ELL) during such disasters.

References [12]–[16] have demonstrated enhanced system resilience through the implementation of planning measures (PMs). These measures involve construction of transmission system equipment to improve system redundancy and reserve capacity. Reference [12] improves system resilience by constructing new transmission lines and substations, reducing the LL during extreme weather events. Moreover, reference [13] explores the effectiveness of the integrated planning of transmission lines, battery storage, and wind farms for mitigation of LL during natural disasters. In [14], LL is minimized during extreme weather events through the systematic planning of transmission lines and distributed energy sources. It not only considered the system resilience requirements during extreme events but also addressed economic needs in normal scenarios. Reference [15] introduces the expected value of the load loss for the worst case (worst-case expected loss - WCEL) as a novel RAI and improved the system's ability to withstand hurricane disasters by planning transmission lines. Reference [16] introduces a novel RAI, namely, capacity accessibility (CA), combined with LL to evaluate system resilience. Enhancement of system resilience was then achieved through the integrated planning of photovoltaic and battery storage.

Additionally, references [17]–[19] enhance system resilience through the implementation of operational measures (OMs). Preventive response measures allow for the scheduling of unit startups, shutdowns, and outputs in advance on the basis of predicted disaster scenarios. Reference [17] introduces a preventive unit commitment model that considers the influence of hurricane disasters. This model is designed to enhance system resilience while mitigating the impact of hurricane disasters on the day-ahead market. Reference [18] introduces a three-stage preventive unit commitment model, wherein the state of the components is categorized into four real-time classifications. The unit scheduling was then refined under different classifications to minimize LL during disasters. Reference [19] introduces a novel preventive scheduling method that considers optimal transmission switching and demand-side management measures to mitigate ELL during hurricanes.

Moreover, in addition to implementing the three types of discussed measures (HMs, PMs, and OMs) individually, references [20]–[24] investigate the impact of the implementation of multiple measures for enhancing system resilience. Reference [20] utilizes ELL as an RAI to selectively implement either HMs or PMs, aiming to enhance system resilience. This is achieved by comparing the cost effectiveness and construction difficulty of different lines. In [21], system resilience is evaluated by assessing ELL, and a four-level distributional robust optimal planning model that combines HMs and PMs is introduced to minimize ELL in the most severe scenarios. Reference [22] introduces a comprehensive resilience assessment framework that encompasses RAIs such as LL, the number of line destructions (NLDs), and transmission capacity loss. The improvements in each index achieved with the implementation of HMs and OMs is subsequently compared. Reference [23] employs HMs and PMs to mitigate system LL during natural disasters, while reference [24] achieves multiple objectives through the construction of new generators and the hardening of transmission lines.

Table I summarizes the work in [9]–[24] from the aspects of natural disasters (ND), resilience enhancement measures (REMs), and RAIs. Among these, NDs include extreme weather events (EWEs) and other disasters, while RAIs include load-related and network-related RAIs. Table I shows that load-related RAIs (LL, ELL, and WCEL) are commonly used to assess system resilience in the current research.

TABLE I
TAXONOMY OF RECENT RESEARCH

Ref	ND		REMs			RAI	
	EWE	Other	HM	PM	OM	LR	NR
[9]	★		★			LL	
[10]	★		★			LL	
[11]	★	★	★			ELL	
[12]	★			★		LL	
[13]	★			★		LL	
[14]	★			★		LL	
[15]	★			★		WCEL	
[16]		★		★		LL	CA
[17]	★				★	LL	
[18]	★				★	LL	
[19]	★				★	ELL	
[20]	★		★	★		LL	
[21]	★		★	★		ELL	
[22]	★		★		★	LL	NLD
[23]	★		★	★		LL	
[24]		★	★	★		LL	
ROTEP	★		★	★	★	CLL	VLSP

Two research gaps are evident from the above assessment:

1) The widely used load-related RAIs do not differ in terms of the importance of loads. Consequently, resilience enhancement schemes are required to protect all loads instead of prioritizing important loads, leading to an imbalance between the resilience and economic considerations of the scheme. In addition, methods based on such indices overlook vulnerable lines within the network. The disconnection of vulnerable lines

during hurricane disasters may trigger multiple failures, further exacerbating system disruption. Consequently, ignoring vulnerable lines within the system may diminish the effectiveness of schemes.

2) Current studies inadequately explore the combined potential of the three resilience enhancement measures (planning measures, hardening measures and operational measures) in the pre-disaster prevention stage of hurricane disasters. Additionally, implementation of planning measures without considering the requirements of normal scenarios may prove uneconomical and unrealistic.

The main contributions of this study are as follows.

1) Two novel RAIs, namely, the combined loss of various classes of loads (CLL) and the vulnerable line survival percentage (VLSP), are proposed to measure the resilience of a system under hurricane conditions.

2) A novel resilience-oriented transmission expansion planning (ROTEP) model is proposed, and three resilience enhancement measures are collaboratively implemented to meet the requirements of normal and hurricane damage scenarios.

The rest of this paper is organized as follows. Section II presents the method for identifying VLs under hurricane conditions. Section III outlines the formulation of the two RAIs and presents the mathematical formulation for the proposed ROTEP model. In Section IV, the proposed model is validated using a modified IEEE RTS-24 and a two-area IEEE RTS-1996, and finally, Section V summarizes the conclusions.

II. Vulnerable line Identification Under Hurricane Conditions

A. Vulnerable Line Identification Based on the Fault Chain Model Under Hurricane Conditions

The failure probability of transmission lines increases during hurricane disasters. Line failures alter the network structure, leading to power flow transfers. As the number of disconnected lines increases, the system becomes significantly more fragile, increasing the risk of cascading failures. These failures follow a cause-and-effect pattern, aligning with the fault chain model [27]. Hence, a fault chain model is adopted to generate fault chains during hurricane disasters.

In this paper, the analysis of fault chains is focused on transmission lines, while excluding transformers and generators as they are less prone to failure during hurricane disasters [28], [29]. For this purpose, this paper utilizes the Batts hurricane model [30], which is a well-established methodology for simulating the dynamic progression of hurricanes. Using the Batts hurricane simulation model, the failure probability of components at various moments is calculated to determine the final component states. The detailed formulas are presented in Appendix (A1) and (A2).

The generation process of fault chains involves three parts 0: identifying the next disconnected chain, determining the termination chain, and computing the risk value associated with the fault chains.

1) Identifying the Next Disconnected Chain

To search for the next disconnected chain, a branch loading assessment index (BLAI) 0 is adopted. The BLAI considers a combination of the deviation and overload degree of the power flow, as well as the corresponding effect on the remaining line after a fault is triggered.

$$\gamma_{w,k+1} = \frac{\left| f_{w,k+1} - f_{w,k} \right|}{f_{w,k+1}^{\max}} \mathrm{e}^{\frac{\left| f_{w,k+1} \right| - f_{w,k+1}^{\max}}{f_{w,k+1}^{\max}}} \tag{1}$$

where $f_{w,k}$ and $f_{w,k+1}$ are the power flows for line w at stages k and k+1 in the fault chain search process, respectively; $f_{w,k+1}^{\max}$ is the maximum limit of the power flow of line w at stage k+1.

In (1), the index $\gamma_{w,k+1}$ has two parts: the function on the left side indicates the power flow deviation of line w after previous outages. A higher value of this function indicates larger fluctuations in the power flow on line w. The exponential function on the right indicates the overload degree of the power flow of line w after previous outages. A higher value of the exponential function indicates a higher likelihood that the power flow of line w will approach or exceed its limit.

By integrating these two parts, the deviation and overload degree of the power flow on line w can be assessed following previous outages. Given that power flow overloads are more prone to causing line outages than power flow deviations, an exponential function is introduced to account for this variation.

2) Determining the Termination Chain and Computing the Value at Risk for the Fault Chains

The termination chains are determined when the fault chains reach a specified length 0:

$$\dim\{\zeta\} = d_{\max} \tag{2}$$

where ζ denotes a fault chain and $d_{\max}$ is the depth of the fault chain prediction.

Upon concluding the search for all fault chains, we calculate the risk for each fault chain individually, and then filter and eliminate those with no risk. The risk of a fault chain occurring is determined by considering both the probability of the fault chain occurrence and the consequences of the resulting damage:

$$\mathrm{Risk}(\zeta) = P(\zeta) \times C(\zeta) \tag{3}$$

$$P(\zeta) = P_{\mathrm{ini}} \prod_{a=1}^{d_{\max}-1} P_a \tag{4}$$

where $C(\zeta)$ is the load shedding for fault chain ζ, which is calculated using the optimal power flow; P_{ini} is the initial probability of a fault being triggered by a

hurricane disaster in fault chain ζ ; P_a is the fault probability of line disconnection in the middle search stage of fault chain ζ . In the *k*th stage of the fault chain search process, if line *m* is the next disconnected line determined on the basis of BLAI calculations after the disconnection of line *n*, then $P_a = \gamma_m$.

3) The Process of Calculating the Risk of a Fault Chain

An example of a fault chain that involves three line outages is used to illustrate the search process. The entire procedure is depicted in Fig. 1.

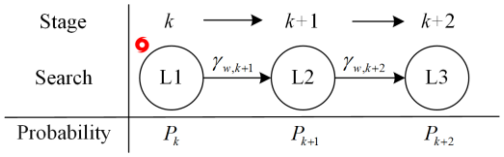

Fig. 1. Fault chain search process.

A fault chain with three line outages corresponds to a total of one initial stage (*k*) and two search stages (*k*+1, *k*+2). In the *k*th stage, suppose that line L1 is damaged and is out of operation due to a hurricane. This results in a change in the entire system network structure, triggering power flow redistribution and initiating the fault chain search process.

Equation (1) is employed to calculate the BLAI for each remaining line and select the line with the highest $\gamma_{w,k+1}$ value as the next outage line (assuming it is L2). In the *k*+1 stage, excluding L2 from the network, the BLAI for each remaining line is calculated, and the line with the highest $\gamma_{w,k+2}$ value is chosen as the outage line in the *k*+2 stage (assuming it is L3). At this point, the fault chain search concludes as the set maximum prediction depth ($d_{\max} = 3$) is reached.

After the fault chain search is concluded, the probability of the fault chain occurring is computed using (4), where the probability of a fault chain occurrence is given by the product of the probabilities of line disconnection at each stage. The fault chain is assumed to be divided into three stages (refer to Fig. 1): in the *k*th stage, L1 is disconnected by a hurricane with a failure probability P_k . In stage *k*+1, L2 is disconnected based on the BLAI after the disconnection of L1. According to 0, the failure probability for L2 is equal to the BLAI, namely, $P_{k+1} = \gamma_{w,k+1}$. Similarly, in stage *k*+2, the failure probability for L3 can be expressed as $P_{k+2} = \gamma_{w,k+2}$.

B. Creating a Cascading Fault Graph

When the method from 0 is applied, all fault chains are transformed into a single entity, namely, a cascading fault graph, which is also a directed weighted graph $G = \{V, E\}$. The nodes $V = \{N_1, N_2, \cdots, N_i\}$ in the cascading fault graph are constructed with lines in the fault chain set, and the edges $E = \{W_1, W_2, \cdots, W_i\}$ are weighted by a combination of BLAIs.

$$W = \sum_{1}^{\aleph} \gamma_w^{\zeta} \Big/ \partial \tag{5}$$

where $\aleph$ is the total number of fault chains, and ∂ is the number of intermediate fault search links in ζ , with a value of $d_{\max} - 1$.

An example is used to illustrate the process of transforming all fault chains into a cascading fault graph. The process is shown in Fig. 2. Suppose that the fault chain set contains a total of four fault chains. For example, fault chain 1 (denoted as FC 1) contains three lines: L1 → L2 → L3. The value of γ_{11} is equal to the value of the BLAI of L2 after the disconnection of L1 and can be computed using (1). After constructing the cascading fault graph in Fig. 2 (right-hand), the weights of the edges can be calculated using (5).

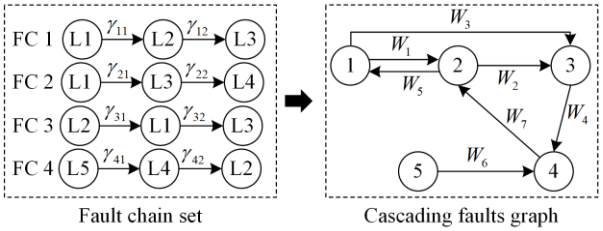

Fig. 2. Cascading fault graph diagramming process.

W_3 , which represents the weight of the edge from Node 1 to Node 3 in the cascading fault graph, is used as an example. Its value is equivalent to the weighted sum of γ for all edges from Node 1 to Node 3 in the fault chain set, i.e., $W_3 = \gamma_{21}/2 + \gamma_{32}/2$. After the fault network graph is drawn, the degree of each node in the graph (e.g., the degree of node 4 is $W_4 + W_6 + W_7$) is calculated, and the nodes are subsequently sorted based on their degree values. The lines corresponding to the nodes with the highest degree values are then identified as vulnerable lines.

C. Vulnerable Line Identification Process

The steps for identifying VLs are as follows.

Step 1: Input relevant information about the transmission system, such as the network, generator, and load data. Input hurricane-related information, such as the initial central pressure difference, speed, landing point, direction. The fault chain set $\Re_{FC}$ and the fault chain ζ^i are initialized.

Step 2: Initialize the count $N = 0$ and the time $t = 0$.

Step 3: Proceed to the next time step ($t = t + 1$). The hurricane simulation model is used to generate initial faults and record all disconnected lines within the fault chain $\zeta^i = \{\{L_1, \cdots, L_j\}\}$. Then, all lines in the fault chain ζ^i are removed from the initial network N_0 , and network $N_0 \rightarrow N_1$ is updated.

Step 4: Check whether $\dim\{\zeta^i\} = d_{\max}$. If true, proceed to Step 5; otherwise, calculate the BLAI for the remaining lines. The line with the highest BLAI is selected as the next disconnected line, and $\zeta_x^i \to \zeta_{x+1}^i == \{\{L_1,...L_j\}, L_j^*\}$ is updated. Subsequently, L_j^* is removed from the current network N_1, network $N_1 \to N_2$ is updated, and the process returns to Step 4.

Step 5: Update fault chain set $\Re_{FC} = \{\zeta^i, \cdots, \zeta^N\}$ and check whether $t < T$ (T denotes the total period of hurricane impact on the network). If true, proceed to Step 6; if not, return to Step 3.

Step 6: Check whether $N < N_{\text{all}}$ (N_{all} represents the predetermined total simulation count). If true, proceed to Step 7; otherwise, return to Step 2.

Step 7: Output the fault chain set $\Re_{\text{FC}}$. The risk value for each fault chain in $\Re_{\text{FC}}$ is calculated using (3), the fault chains with a risk value of 0 are eliminated, and a cascading fault graph is constructed to identify the VLs.

III. Problem Formulation

A. Resilience Assessment Index

Hurricanes may damage multiple transmission lines, weakening network functionality and resulting in load loss. Previous studies often used the overall LL 0,0 to reflect the extent of systemic performance decline during hurricane disasters. On this basis, this paper categorizes the load into three levels (very important, important, and general) and proposes the post-disaster combined loss of various classes of loads (CLL) as an RAI, given as:

$$L_{\text{CLL}} = \sum_{d_s}\sum_{t}^{T}\sum_{b}^{N_{\text{B}}}\sum_{i}^{3} \varpi_i p_{\text{ls},b,t,i}\Delta t \tag{6}$$

where d_s denotes the hurricane damage scenario; and ϖ_i represents the weight of the ith class load; T denotes the total period of the hurricane impact on the network; N_{B} denotes the total number of buses; and $p_{\text{ls},b,t,i}$ represents the load loss of the ith class. While the CLL reflects the post-disaster load loss situation, using it alone as an RAI may not effectively capture hurricane damage to VLs. Therefore, we propose the vulnerable line survival proportion (VLSP) as another resilience index, as:

$$P_{\text{VLSP}} = \sum_{d_s}\omega_{d_s}\left(\frac{\psi - \xi_{d_s}}{\psi}\right) \tag{7}$$

where ω_{d_s} represents the probability of occurrence of scenario d_s; ψ denotes the total number of VLs within the system; while ξ_{d_s} denotes the number of VLs damaged in scenario d_s.

B. Model Formulation

This section presents the mathematical formulation of the proposed ROTEP model. The ROTEP model integrates line planning, hardening, and the coordinated operation of units with battery energy storage systems (BESSs) as REMs. The model is divided into two stages, where the objective of the first-stage model is to address the increasing load demand by constructing new lines.

1) First-stage Model

$$\min \sum_{l\in\Gamma^*} c_l x_l + \sum_{s_s=1}^{N_S}\omega_{s_s}\sum_{t=1}^{T_D}\left\{\sum_{g=1}^{N_G}\left(\begin{array}{l} O_g^{\text{C}} P_{\text{G},g,t,s_s} + O_g^{\text{open}} v_{\text{G},g,t,s_s} + \\ O_g^{\text{down}} w_{\text{G},g,t,s_s}\end{array}\right) + \right.$$
$$\left.\sum_{e=1}^{N_E} O_e^{\text{C}}\left(P_{\text{eD},e,t,s_s} + P_{\text{eC},e,t,s_s}\right) + \left(\rho_{\text{ls}}\sum_{b=1}^{N_B} p_{\text{ls},b,t,s_s} + \rho_{\text{wc}}\sum_{r=1}^{Nw} p_{\text{wc},r,t,s_s}\right)\right\} \tag{8}$$

The objective function (8) contains four parts: namely, the cost of line construction, operating cost of units, maintenance cost of BESSs, and penalty cost for wind abandonment and load loss, respectively. Where c_l represents the planning cost of line l; x_l is a binary variable; and $x_l = 1$ indicates that line l is constructed; while Γ^* represents the set of candidate lines; N_S, T_D, and N_G represent the number of typical normal scenarios, the total number of periods for each typical normal scenario, and the total number of generators, respectively; ω_{s_s} represents the probability of a typical normal scenario s_s occurring; O_g^{C} represents the fuel cost coefficient for generator g; and P_{G,g,t,s_s} represents the output of generator g at time t in scenario s_s; O_g^{open} and O_g^{down} represent the startup and shutdown costs for generator g, respectively; v_{G,g,t,s_s} and w_{G,g,t,s_s} represent the startup and shutdown status variables for generator g at time t in scenario s_s, respectively, while $v_{\text{G},g,t,s_s} = 1$ indicates that generator g starts at time t in scenario s_s; N_E represents the total number of BESSs; O_e^{C} represents the maintenance cost for BESS e; while P_{eD,e,t,s_s} and P_{eC,e,t,s_s} represent the discharge and charge power of BESS e at time t in scenario s_s, respectively; N_{B} and N_{W} represent the total number of bus nodes with load and wind power generation, respectively; ρ_{ls} and ρ_{wc} represent the penalty costs for load loss and wind curtailment, respectively; p_{ls,b,t,s_s} represents the load curtailment of bus b at time t in scenario s_s; and p_{wc,r,t,s_s} represents the curtailed wind power of wind power generation r at time t in scenario s_s.

$$\sum_{g} P_{\text{G},g,t,s_s} + \sum_{r}(P_{\text{Re},r,t,s_s}^{\max} - p_{\text{wc},r,t,s_s}) + \sum_{\forall m,n\in l} P_{l(mn),t,s_s} + \sum_{e} P_{\text{eD},e,t,s_s} - \sum_{e} P_{\text{eC},e,t,s_s} = p_{\text{d},b,t,s_s} - p_{\text{ls},b,t,s_s} \tag{9}$$

Equation (9) expresses the power balance constraint

for each bus, where $P_{\mathrm{Re},r,t,s_s}^{\max}$ represents the maximum output of wind power generation r at time t in scenario s_s; $P_{l(mn),t,s_s}$ represents the active power flow on line l at time t in scenario s_s (where line l connects buses m and n); and p_{d,b,t,s_s} represents the total load on bus b at time t in scenario s_s.

$$x_l f_{l,t,s_s}^{\min} \leqslant P_{l,t,s_s} \leqslant x_l f_{l,t,s_s}^{\max} \tag{10}$$

$$\left|P_{l,t,s_s} - B_l\left(\theta_{l(m),t,s_s} - \theta_{l(n),t,s_s}\right)\right| \leqslant \mathrm{M}*(1-x_l) \tag{11}$$

Equations (10) and (11) describe the line capacity and DC power flow constraints, respectively, where $f_{l,t,s_s}^{\max}$ and $f_{l,t,s_s}^{\min}$ denote the upper and lower transmission capacity limits of line l at time t in scenario s_s, respectively; B_l is the reactance of line l; and M is a very large positive number; $\theta_{l(m),t,s_s}$ and $\theta_{l(n),t,s_s}$ represent the phase angles at buses m and n for line l at time t in scenario s_s, respectively. For existing lines, x_l is always equal to 1.

$$0 \leqslant p_{\mathrm{ls},b,t,s_s} \leqslant p_{\mathrm{d},b,t,s_s} \tag{12}$$

$$P_{\mathrm{Re},r,t,s_s}^{\min} \leqslant p_{\mathrm{wc},r,t,s_s} \leqslant P_{\mathrm{Re},r,t,s_s}^{\max} \tag{13}$$

Equations (12) and (13) constrain the load loss and the curtailed wind power within a certain range, respectively, where $P_{\mathrm{Re},r,t,s_s}^{\max}$ and $P_{\mathrm{Re},r,t,s_s}^{\min}$ represent the maximum and minimum output powers of wind power generation r at time t in scenario s_s, respectively.

$$u_{\mathrm{G},g,t,s_s} P_{\mathrm{G},g,t,s_s}^{\min} \leqslant P_{\mathrm{G},g,t,s_s} \leqslant u_{\mathrm{G},g,t,s_s} P_{\mathrm{G},g,t,s_s}^{\max} \tag{14}$$

Equation (14) describes the constraint on the output of the thermal power generator, where $P_{\mathrm{G},g,t,s_s}^{\max}$ and $P_{\mathrm{G},g,t,s_s}^{\min}$ are the maximum and minimum output powers, respectively, of generator g at time t under scenario s_s; u_{G,g,t,s_s} represents the status variable of generator g at time t in scenario s_s; and $u_{\mathrm{G},g,t,s_s}=1$ indicates that generator g is in operation; otherwise, it is in a shutdown state.

$$P_{\mathrm{G},g,t,s_s} - P_{\mathrm{G},g,t-1,s_s} \leqslant \delta_{g,\mathrm{up}} \tag{15}$$

$$P_{\mathrm{G},g,t-1,s_s} - P_{\mathrm{G},g,t,s_s} \leqslant \delta_{g,\mathrm{down}} \tag{16}$$

Equations (15) and (16) describe the ramp-up and ramp-down constraints of the generator, where $\delta_{g,\mathrm{up}}$ and $\delta_{g,\mathrm{down}}$ denote the upward and downward rates of generator g, respectively.

$$\sum_{g=1}^{N_G}\left(u_{\mathrm{G},g,t,s_s} P_{\mathrm{G},g,t,s_s}^{\max} - P_{\mathrm{G},g,t,s_s}\right) \geqslant \beta \sum_{b=1}^{N_B} p_{\mathrm{d},b,t,s_s} \tag{17}$$

Equation (17) is the spinning reserve constraint, where β represents the reserve coefficient.

$$-u_{\mathrm{G},g,t-1,s_s} + u_{\mathrm{G},g,t,s_s} - u_{\mathrm{G},g,\tau,s_s} \leqslant 0,\ \forall \tau \in \left\{t,\cdots,T_g^{\mathrm{SU}}+t-1\right\} \tag{18}$$

$$u_{\mathrm{G},g,t-1,s_s} - u_{\mathrm{G},g,t,s_s} + u_{\mathrm{G},g,\tau,s_s} \leqslant 1,\ \forall \tau \in \left\{t,\cdots,T_g^{\mathrm{SD}}+t-1\right\} \tag{19}$$

Equations (18) and (19) are constraints on the minimum start-up and shut-down times for the generator, where T_g^{SU} and T_g^{SD} denote the minimum durations after the start-up and shut-down of the generator, respectively.

$$v_{\mathrm{G},g,t,s_s} + w_{\mathrm{G},g,t,s_s} \leqslant 1 \tag{20}$$

$$v_{\mathrm{G},g,t,s_s} - w_{\mathrm{G},g,t,s_s} = u_{\mathrm{G},g,t,s_s} - u_{\mathrm{G},g,t-1,s_s} \tag{21}$$

$$v_{\mathrm{G},g,t,s_s}, w_{\mathrm{G},g,t,s_s}, u_{\mathrm{G},g,t,s_s} \in \{0,1\} \tag{22}$$

Equations (20)–(22) impose constraints on the start-up and shut-down state variables of the unit. Equation (20) prohibits the unit from starting and shutting down simultaneously; equation (21) describes the relationship between the operating status of the unit and the start-up and shut-down state variables; and equation (22) indicates that the operating, start-up, and shut-down state variables are all binary.

$$u_{\mathrm{eC},e,t,s_s} P_{\mathrm{eC},e}^{\min} \leqslant P_{\mathrm{eC},e,t,s_s} \leqslant u_{\mathrm{eC},e,t,s_s} P_{\mathrm{eC},e}^{\max} \tag{23}$$

$$u_{\mathrm{eD},e,t,s_s} P_{\mathrm{eD},e}^{\min} \leqslant P_{\mathrm{eD},e,t,s_s} \leqslant u_{\mathrm{eD},e,t,s_s} P_{\mathrm{eD},e}^{\max} \tag{24}$$

Equations (23)–(24) constrain the charging and discharging power of the BESS to within certain limits, where $P_{\mathrm{eC},e}^{\max}$ and $P_{\mathrm{eC},e}^{\min}$ represent the maximum and minimum charging power, respectively, of BESS e; $P_{\mathrm{eD},e}^{\max}$ and $P_{\mathrm{eD},e}^{\min}$ represent the maximum and minimum discharging power, respectively, of BESS e; u_{eC,e,t,s_s} and u_{eD,e,t,s_s} represent the charging and discharging state variables, respectively, of BESS e at time t in scenario s_s.

$$E_e^{\min} \leqslant E_{e,t,s_s} \leqslant E_e^{\max} \tag{25}$$

$$E_{e,t,s_s} = E_{e,t-1,s_s} + P_{\mathrm{eC},e,t,s_s}\eta_{e,\mathrm{pch}} - P_{\mathrm{eD},e,t,s_s}/\eta_{e,\mathrm{pdch}} \tag{26}$$

$$E_{e,0,s_s} = E_{e,T,s_s} \tag{27}$$

Equation (25) describes the total energy constraint of BESS e, where $E_e^{\max}$ and $E_e^{\min}$ represent the upper and lower limits of the total energy of BESS e, respectively; and E_{e,t,s_s} represents the energy of BESS e at time t in scenario s_s. Equation (26) constrains the power and energy conversion of BESS e, where $\eta_{e,\mathrm{pch}}$ and $\eta_{e,\mathrm{pdch}}$ represent the charging and discharging efficiency of BESS e, respectively. Equation (27) ensures that, for the BESS, the energy at the initial and final times is the same.

2) Second-stage Model

The first-stage model is a transmission expansion planning (TEP) model that considers the requirements

of normal scenarios. The objective is to devise a planning scheme that accommodates both load growth and uncertainty of renewable energy. The limitations of the model lie in the resulting scheme's insufficient resilience to disasters, primarily attributed to the lack of consideration of potential hurricane disasters. Building on this foundation, this paper addresses the limitations of the TEP model by introducing a second-stage model. Then, the implementation of hardening measures enhances the scheme's resilience under hurricane scenarios. By building on the initial planning scheme (IPS) derived from the first-stage model, VLs susceptible to hurricane disasters are identified. On the basis of the first-stage planning scheme, VLs undergo systematic strengthening through HMs (if necessary) to further improve the VLSP in the second-stage model. To address the uncertainty associated with hurricane disasters throughout the planning period, various damage scenarios are generated using the Monte Carlo sampling technique. The aggregate contribution of each line is then computed across all hurricane damage scenarios.

$$\Delta L_{\mathrm{CLL}-l,d_s} = L_{\mathrm{CLL-IPS},d_s} - L_{\mathrm{CLL}}\Big|_{\mathrm{IPS}\cup(h_l=1),d_s} \quad l \in \Xi \tag{28}$$

$$\begin{aligned} &\Delta L_{\mathrm{CLL}-l,d_s} = L_{\mathrm{CLL-IPS},d_s} - L_{\mathrm{CLL}}\Big|_{\mathrm{IPS}\cup(h_l=1),d_s}, \quad l \in \Xi \\ &T_{\mathrm{C}_l^{\mathrm{CLL}}} = \sum_{d_s} \Delta L_{\mathrm{CLL}-l,d_s} \end{aligned} \tag{29}$$

where $\Delta L_{\mathrm{CLL}-l,d_s}$ represents the increase in the CLL resulting from the hardening of line l in hurricane scenario d_s; $L_{\mathrm{CLL-IPS},d_s}$ represents the CLL under the IPS in hurricane scenario d_s;and $L_{\mathrm{CLL}}\big|_{\mathrm{IPS}\cup(h_l=1),d_s}$ denotes the CLL when line l is assumed to be hardened in hurricane scenario d_s (assuming that line l is assumed to have 100% reliability under all hurricane scenarios); $T_{\mathrm{C}_l^{\mathrm{CLL}}}$ signifies the overall enhancement in the CLL resulting from the hardening of vulnerable line l across all hurricane scenarios. On this basis, the second-stage model is formulated as follows:

$$\begin{aligned} \min \sum_{t=1}^{T_D} \Bigg\{ &\sum_{g=1}^{N_G} \left(O_g^{\mathrm{C}} P_{\mathrm{G},g,t,d_s} + O_g^{\mathrm{open}} v_{\mathrm{G},g,t,d_s} + O_g^{\mathrm{down}} w_{\mathrm{G},g,t,d_s} \right) + \\ &\sum_{e=1}^{N_E} O_e^{\mathrm{C}} \left(P_{\mathrm{eD},e,t,d_s} + P_{\mathrm{eC},e,t,d_s} \right) \Bigg\} + \sum_{t}^{T} \sum_{b}^{N_{\mathrm{B}}} \sum_{i}^{3} \lambda_i p_{\mathrm{ls},b,t,i,d_s} \Delta t \end{aligned} \tag{30}$$

The objective function (30) contains three parts: namely, the operating cost of the generator, the maintenance cost of the BESS, and the penalty cost for different classes of loads in hurricane scenario d_s, respectively, where λ_i signifies the penalty cost for shedding the load of the ith class; while $p_{\mathrm{ls},b,t,i,d_s}$ is the magnitude of the shed load for the ith class at bus b.

$$(z_l + v_{l,d_s} - z_l v_{l,d_s}) f_{l,t,d_s}^{\min} \leqslant P_{l,t,d_s} \leqslant f_{l,t,d_s}^{\max} (z_l + v_{l,d_s} - z_l v_{l,d_s}) \tag{31}$$

$$\left| P_{l,t,d_s} - B_l (\theta_{l(m),t,d_s} - \theta_{(n),t,d_s}) \right| \leqslant M * (1 - (z_l + v_{l,d_s} - z_l v_{l,d_s})) \tag{32}$$

where v_{l,d_s} indicates whether line l is damaged in hurricane scenario d_s, if $v_{l,d_s} = 0$, line l is damaged; z_l indicates whether line l is hardened, if $z_l = 1$, line l is hardened, signifying that it will not succumb to damage during a hurricane. For this segment, $(z_l + v_{l,d_s} - z_l v_{l,d_s})$ signifies that line l is deactivated only when it is damaged by a hurricane ($v_{l,d_s} = 0$) and remains unhardened ($z_l = 0$).

The wind speed varies during a hurricane, and the output of the wind generator is determined through the use of wind speed curves [34]:

$$P_v = \begin{cases} 0, \ 0 \leqslant v \leqslant v_{\mathrm{in}} \\ (A + Bv + Cv^2) P_r, \ v_{\mathrm{in}} \leqslant v \leqslant v_{\mathrm{r}} \\ P_r, \ v_{\mathrm{r}} \leqslant v \leqslant v_{\mathrm{out}} \\ 0, \ v \geqslant v_{\mathrm{out}} \end{cases} \tag{33}$$

where v_{in} represents the cut-in wind speed; v_{r} represents the rated wind speed; v_{out} represents the cut-out wind speed; P_r represents the rated power of the wind generator; and A, B, and C are coefficients, which are calculated as follows:

$$A = \frac{v_{\mathrm{in}}(v_{\mathrm{in}} + v_{\mathrm{r}}) - 4(v_{\mathrm{in}} v_{\mathrm{r}}) \left(\dfrac{v_{\mathrm{in}} + v_{\mathrm{r}}}{2v_{\mathrm{r}}} \right)^3}{(v_{\mathrm{in}} - v_{\mathrm{r}})^2}$$

$$B = \frac{4(v_{\mathrm{in}} + v_{\mathrm{r}}) \left(\dfrac{v_{\mathrm{in}} + v_{\mathrm{r}}}{2v_{\mathrm{r}}} \right)^3 - (3v_{\mathrm{in}} + v_{\mathrm{r}})}{(v_{\mathrm{in}} - v_{\mathrm{r}})^2}$$

$$C = \frac{2 - 4 \left(\dfrac{v_{\mathrm{in}} + v_{\mathrm{r}}}{2v_{\mathrm{r}}} \right)^3}{(v_{\mathrm{in}} - v_{\mathrm{r}})^2}$$

The remaining constraints are the same as those in the first-stage model, namely, equations (9) and (12)–(27). The ROTEP model proposed in this paper is a two-stage model, and the two-layer model can be solved sequentially. The first stage involves solving a mixed-integer linear programming (MILP) problem, and the second stage involves solving a linear programming (LP) problem combined with heuristic search strategies. Considering the characteristics of our proposed model, when the proposed method is applied to large power systems, although the solution efficiency may decrease to some extent, convergence issues are generally not encountered.

C. The Whole Process of the Proposed Model

The solution process for the proposed ROTEP model is divided into four steps, as depicted in Fig. 3.

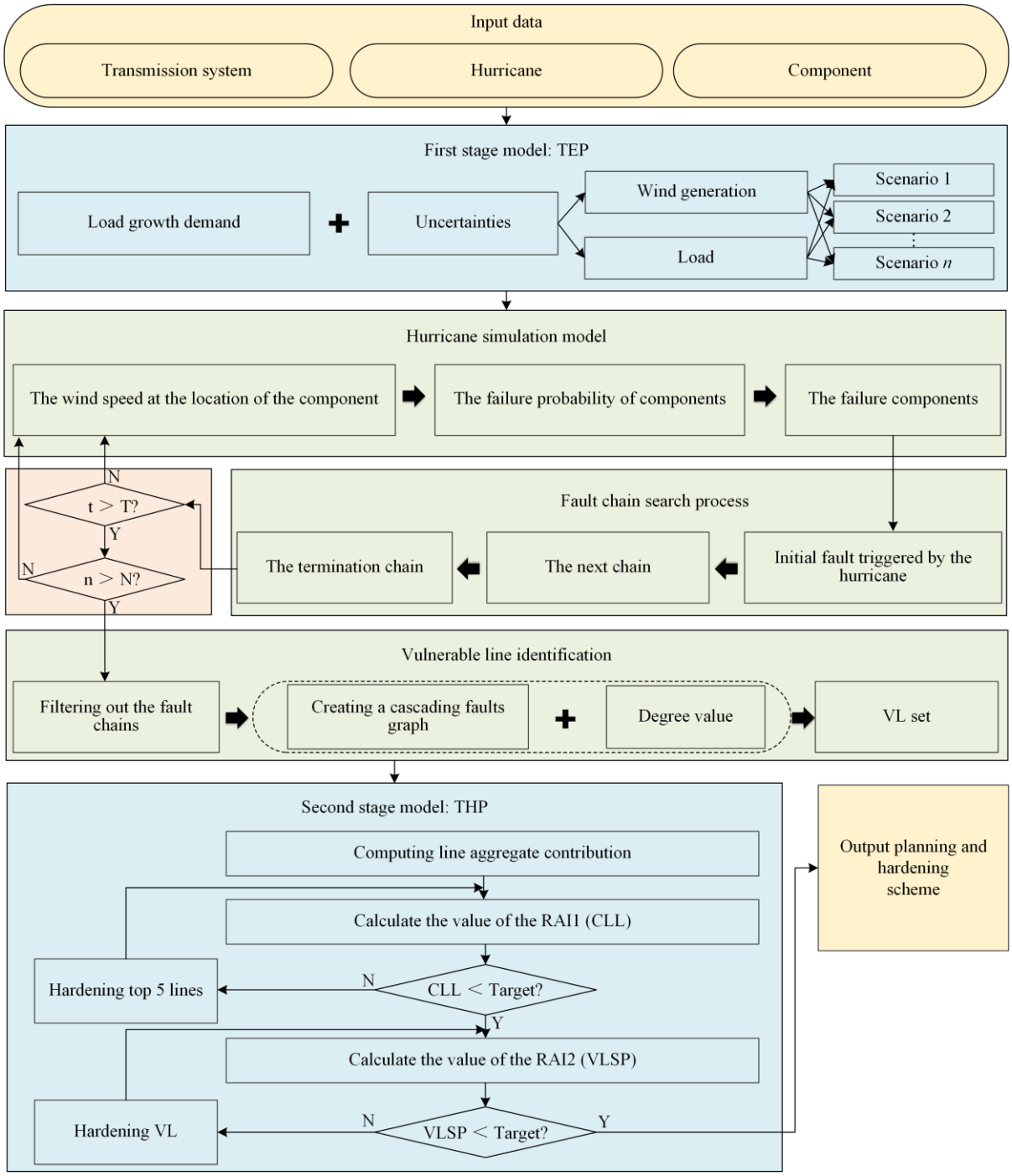

Fig. 3. Entire process of the ROTEP model.

Step 1: Input the data, including the transmission network data and hurricane parameter data. The transmission network data include the planning and hardening costs of the lines, the output costs and installed capacities of the generators, and the loads and geographic coordinates of the buses. The hurricane parameter data encompass the initial central pressure difference, landing point, movement speed, and path of the hurricane.

Step 2: The first-stage models are solved to derive a planning scheme that meets the load increase requirement. Subsequently, VLs are identified using the method outlined in subsection II.C.

Step 3: Multiple samplings of key hurricane parameters are conducted to generate a set of hurricane damage scenarios. For each scenario, the second-stage model is solved to determine the CLL value and verify that the CLL value is below the predefined target. If the CLL values for all of the scenarios meet the relevant requirements, proceed to Step 4. Otherwise, the improvement values for the CLLs in all hurricane scenarios are calculated by (28) and (29). The top several lines

with the highest values are hardened, and this process is repeated until the CLLs meet the predefined targets. Then, proceed to Step 4.

Step 4: Evaluate whether the VLSP exceeds the predefined target. If the VLSP values meet the requirements for all scenarios, the line hardening scheme is output. Otherwise, the damaged and unhardened VLs are organized in descending order of cost, and the least costly VLs are hardened one by one until the VLSP satisfies the requirements. Finally, the line hardening scheme is output.

IV. Case Study

All programming is carried out using MATLAB R2022a software, and mature commercial solvers GUROBI and YALMIP are used. The proposed ROTEP model is applied to a modified IEEE RTS-24 system [35] and a two-area IEEE RTS-1996 system [36].

To implement the planning measures based on the increased demand due to load growth in normal scenarios while accounting for uncertainties in the wind generation output and load, the k-cluster algorithm is employed.

This algorithm yields four typical normal scenarios, and the 24-hour fluctuations in the wind generation output and load for each scenario are depicted in the appendix (see Figs. C1 and C2). The initial data are derived from [37]. To implement hardening measures to increase system resilience and address the requirements for damage scenarios, the hurricane evolution process is simulated for the geographic wiring diagram of an IEEE RTS-24 system shown in Fig. 4, with the specific parameters referenced from [38].

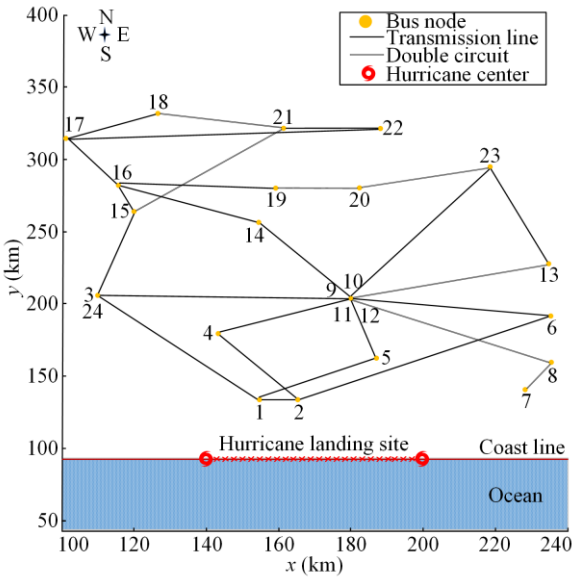

Fig. 4. Geographic wiring diagram of the IEEE RTS-24.

The abbreviations used in Section IV are summarized in Table II.

TABLE II
Explanations of Abbreviations in Section 4

Abbreviation	Meaning	Unit
NHL	Number of hardened lines	
L_{VIT}	Very important load	
L_{IT}	Important load	
L_G	General load	
HC	Hardening cost	$\$10^6$
OC	Operation cost	$\$10^6$
PEL	Power energy loss	MWh
PELC	Power energy loss cost	$\$10^6$
TC	Total cost	$\$10^6$

To consider the uncertainty associated with hurricane disasters during the planning stage, simulations are conducted for a total of 50 random hurricanes. The number 50 is chosen based on the central meteorological observatory database [39], which recorded approximately 50 hurricanes making landfall in China over the past 20 years. The progression of hurricanes is simulated using the Batts hurricane model. This hurricane model is implemented through the temporal variation of key parameters, such as the initial central pressure difference, the angle between the direction of hurricane motion and the coastline and the translation speed. These initial hurricane parameters are acquired by sampling from respective probability distributions [38]. The landing site is assumed to be within the coastline coordinate range of 145–160, as depicted in Fig. 4.

A. Modified IEEE RTS-24

The proposed model undergoes initial validation using the modified IEEE RTS-24. This example contains 24 bus nodes with an aggregate load of 2850 MW, 33 generators with a combined installed capacity of 3405 MW, and 38 transmission lines. The combined installed capacities of generators and loads are increased by a factor of 1.5 to simulate load growth in the target planning year. Additionally, a transmission line is incorporated into the 7-8 corridor to ensure compliance with the *N*-1 criterion. Simultaneously, an installed capacity of 600 MW of wind power and 100 MW/200 MWh of BESS [40] are established at each of the 3rd and 19th bus nodes, respectively. The BESS has charging and discharging efficiencies of 0.9.

1) Comparison of Schemes Across Various Hardened Lines

The research gap arising from the incomplete consideration of load importance in the development of REMs, which results in an imbalance between TCs, is explored to achieve resilience improvement in planning schemes. The PELs for different classes of loads under various schemes are illustrated in Fig. 5.

Figure 5 clearly indicates that as the NHLs increase, there is a consistent decreasing trend in the sum of PELs across all classes of loads for all hurricane scenarios. The most significant reduction in the sum of the PELs

across various classes of loads in all hurricane disaster scenarios occurs before the NHLs reach 10.

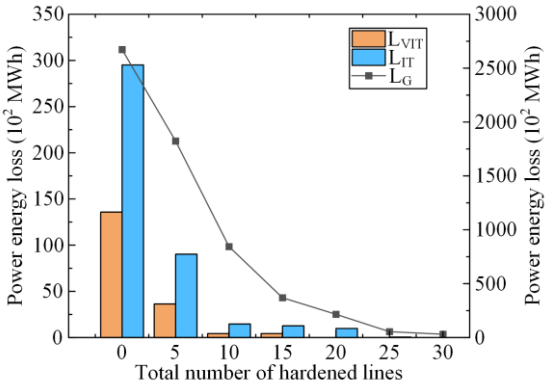

Fig. 5. PELs for different loads in various schemes.

Then, a further hardening of the line primarily contributes to the decrease in L_G. The associated PEL for each class of load and the CLL for each scenario with varying NHLs are presented in Table III.

TABLE III
PEL AND CLL FOR DIFFERENT HARDENING SCHEMES

NHL	PEL (MWh)			CLL (MWh)
	L_{VIT}	L_{IT}	L_G	
0	13 575	29 508	267 196	42 123.8
5	3637	9023	182 341	22 584.4
10	424	1468	84 394	9029.8
15	424	1272	36 925	4243.7
20	0	980	21 559	2351.9
25	0	47	8465	855.9
30	0	0	3092	309.2

As the NHL increases, the resilience of the CLL RAI continues to decrease, but the rate of decline diminishes. To further evaluate the economic merits and drawbacks of hardening schemes with different NHLs, Table IV presents the corresponding TCs, and the trends are illustrated in Fig. 6. The TC includes both the HC of the line and the penalty PELC across various load classes.

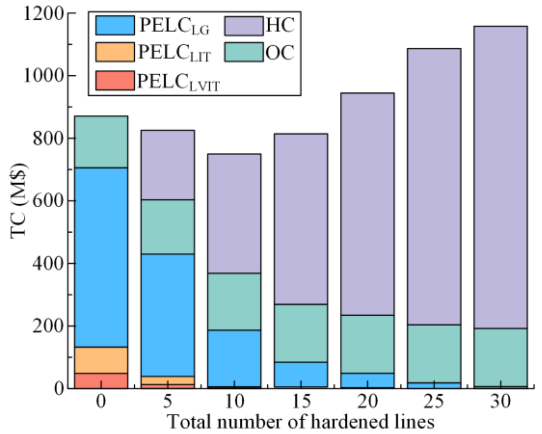

Fig. 6. TCs for various schemes.

TABLE IV
COSTS OF SCHEMES UNDER DIFFERENT NHLS

NHL	PELC ($10^6)			OC ($10^6)	HC ($10^6)	TC ($10^6)
	L_{VIT}	L_{IT}	L_G			
0	48.5	84.3	572.6	165.3	0	870.7
5	13.0	25.8	390.7	173.9	222	825.4
10	1.5	4.2	180.8	182.1	381	749.7
15	1.5	3.6	79.1	184.8	545	814.1
20	0	2.8	46.2	185.4	710	944.4
25	0	0.1	18.1	185.6	883	1086.8
30	0	0	6.6	185.4	966	1158.0

As depicted in Fig. 6, the TC of the hardening scheme initially decreases and subsequently increases as the NHL continues to increase. This is because in the initial stage of line hardening, the transmission network's resilience to hurricanes significantly improves, leading to a substantial reduction in the PELC for different loads. When the NHL is increased to 5, compared to that for NHL equaling 0, the total penalty PELC is reduced by 275.9 $\$10^6$, the cost of the hardening scheme increases by 222 $\$10^6$, and the TC is reduced by 45.3 $\$10^6$, or 5.2%. When the NHL is increased from 5 to 10, the TC of the hardening scheme decreases by 75.7 $\$10^6$, or 9.2%.

As the NHL increases, there is a marginal diminishing effect on the subsequent contribution of these hardened lines to reductions in various classes of load. In other words, despite the subsequent hardening of the same number of lines, this contribution to reducing various classes of load loss decreases compared to that for initial hardening. For instance, when the NHL increases from 10 to 15, the HC increases by 164 $\$10^6$ However, the total penalty PELC decreases by only 102 $\$10^6$, and the OCs remain essentially unchanged. Consequently, the TC increases by 64.4 $\$10^6$. The TC of the hardening scheme then begins to increase, and this trend becomes more noticeable as the NHL increases.

To emphasize the importance of distinguishing load priorities in the implementation of hardening measures and considering practical situations, ensuring zero load loss during hurricane disasters is a substantial challenge.

We establish four comparative scenarios, and the critical points are presented in Table V, where S1–S3 account for the differences in load importance and S4 does not. The first three scenarios (S1–S3) involve varying upper limits for the total allowable PEL across different classes of loads. By contrast, in S4, the load importance is not accounted for, and the total allowable PEL serves as the upper limit for all loads. Using the second row (S1) as an example, the upper limit of the total allowable PEL for the LVIT in all disaster scenarios is set to 513 MWh.

TABLE V
ALLOWABLE PEL CRITERIA FOR DIFFERENT LOADS

Scenario	Aspect	Upper limit of total allowable PEL (MWh)
S1	L_{VIT}	513
S2	L_{IT}	1026
S3	L_G	3591
S4	All loads	5130

Following the different total allowable PEL limitations, the corresponding hardening schemes for scenarios S1–S4 are as follows: the NHL values are 10, 20, 30, and 30, respectively. According to Table IV, the TCs for scenarios S1–S4 are 749.7, 944.4, 1158, and 1158 M$, respectively. In summary, distinguishing load importance provides economic advantages compared to a method that does not make such distinctions in the hardening scheme.

2) Comparing Hardening Schemes with and without Identifying Vulnerable Lines

This research gap arises from the incomplete consideration of protecting VLs during the formulation of REMs. Based on the fault chain simulation method introduced in Section II, a set of more than 8000 fault chains is generated; then, the risk index is utilized to filter the fault chain set, yielding a total of more than 2700 fault chains. The remaining fault chains are employed to construct a cascading fault graph and identify VLs. In this paper, the length of each fault chain is fixed at 3.

Notably, each segment in the remaining fault chain is a single line. Specifically, we filter out fault chains for which the initial fault is composed of multiple lines. This is attributed to the likelihood that hurricane disasters induce multiple failures, indicating that an initial fault may be caused by the simultaneous disconnection of multiple lines during the fault chain search process. Nevertheless, in the computation of the degree values for all nodes in the cascading fault graph, nodes comprising multiple lines present a lower degree value than other nodes. Therefore, in this paper, we exclusively focus on fault chains for which each segment corresponds to a single line.

The cascading fault graph for RTS-24 is shown in Fig. 7, and the normalized degree values of all of the lines post-sorting are depicted in Fig. 8.

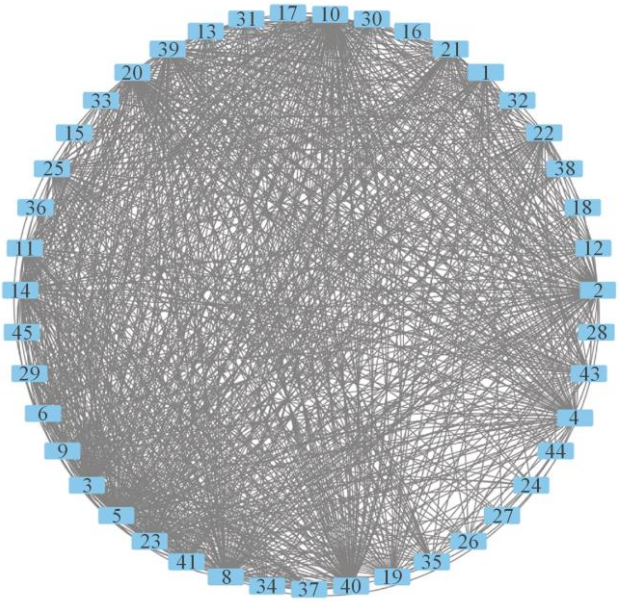

Fig. 7. Cascading faults for RTS-24.

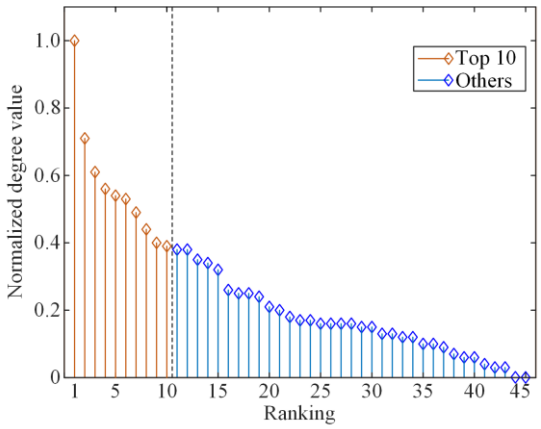

Fig. 8. Results of the line normalized degree value calculation.

In this paper, the top 10 lines with the highest normalized degree values are identified as VLs, and these lines serve as targets for the subsequent hardening schemes. Table VI provides the specific normalization degree values for the top 10 lines.

TABLE VI
NORMALIZED DEGREE VALUES FOR THE TOP 10 LINES

Rank	Line	NDV	Rank	Line	NDV
1	6-10	1.000	6	8-10	0.531
2	2-6	0.709	7	4-9	0.493
3	5-10	0.605	8	7-8	0.437
4	1-5	0.559	9	11-13	0.404
5	1-5	0.543	10	1-2	0.387

Once the CLL condition is satisfied, consideration is given to enhancing the VLSP based on the actual demand. Using S1 with NHL equaling 10 from Table IV as an example, additional hardening measures are implemented, and the comparative results are presented in Table VII.

TABLE VII
COMPARISON OF HARDENING SCHEMES (S1 VS. S1*)

	S1	S1*
NHL	10	14
HC (10^6)	381	497
PELC (10^6)	186.5	117.8
OC(10^6)	182.1	183.9
TC (10^6)	749.7	798.7
VLSP (%)	84.2	100

Table VII reveals that the VLSP can be enhanced from 84.2% to 100% by incorporating four new lines into scheme S1* compared to S1. The HC of S1* increases by 116 10^6. However, owing to the network improvement, the PELC experiences a reduction of 68.7 10^6, resulting in a net increase of only 49 10^6 in the TC, or approximately 6.5%. In practice, the decision to implement additional hardening measures tailored to the increase in VLSPs can be made on demand.

3) Comparing Schemes with Other Indices

We compare the results of other assessment indices adopted in previous studies [20], [30], such as load loss

(LL). The comparison case is established as follows:

Case 1 (C1): Consider only the LL as an RAI.

ROTEP (C2): Consider both the CLL and VLSP as two RAIs.

Table VIII indicates that for the same number of NHLs, the scheme obtained based on C2 improves the VLSP by 13.8% compared to that obtained for C1. This improvement is accompanied by a total cost increase of approximately 16.4 $\$10^6$, corresponding to approximately 2.1%. In addition, both schemes can reduce the PELC to some extent through the construction of new lines. Specifically, compared to C2, C1 is slightly more effective in reducing PELC, achieving an additional reduction of approximately 3.6 $\$10^6$, or approximately 3.2%.

TABLE VIII
COMPARISON OF HARDENING SCHEMES (C1 VS. C2)

	C1	C2
NHL	14	14
HC ($\$10^6$)	484	497
PELC ($\$10^6$)	114.2	117.8
OC ($\$10^6$)	184.1	183.9
TC ($\$10^6$)	782.3	798.7
VLSP (%)	86.2	100

4) Comparing Schemes with and without BESSs

To investigate the influence of BESSs as emergency resources on the PEL for different classes of loads during hurricane disasters. The scenario with NHL equaling 0 (denoted as S0) from Table IV is used as an example, and the comparison scenario S5 is established, with a BESS at bus 10 and NHL equaling 0. A comparison of the results is presented below.

According to Table IX, the introduction of a BESS as an emergency resource leads to a reduction in the PEL for all classes of loads. Compared with S0, S5 reduces the PEL for L_{VIT}, L_{IT}, and L_G by 551 MWh, 1076 MWh, and 6459 MWh, corresponding to approximately 4.1%, 3.6%, and 2.4%, respectively. Additionally, the resilience index of the CLL decreases by 1246.9 MWh, or approximately 3.0%. Bus 10 exhibited the most substantial reduction in PEL, with a decrease of 3457 MWh, constituting 42.8% of the overall PEL reduction.

TABLE IX
COMPARISON OF HARDENING SCHEMES (S0 VS. S5)

	PEL (MWh)			CLL (MWh)
	L_{VIT}	L_{IT}	L_G	
S0	13 575	29 508	267 196	42 123.8
S5	13 024	28 432	260 737	40 876.9

B. Modified Two-area IEEE RTS-1996

The modified two-area IEEE RTS-1996 is a larger system used to demonstrate the effectiveness of the proposed ROTEP model. The case consists of two regions with a total of 71 transmission lines, 5700 MW of overall load, and 6810 MW of generator capacity. The following modifications are implemented: the thermal power capacity and load demand are increased to 1.5 times their initial values. One new transmission line is introduced for corridor 7–8, and the other is introduced for corridor 31–32. Wind farms are linked to buses 3 and 19 in region 1 and buses 27 and 43 in region 2, all with initial capacities of 600 MW. The connection locations of the four BESSs align with those of the four wind farms. The remaining information for each region is identical to that for IEEE RTS-24. The geographic wiring diagram of the two-area IEEE RTS-1996 system is introduced in Fig. D1. The landing site is assumed to be within the coastline coordinate range of 200–320. Table X displays the CLL and TC values corresponding to the hardening scheme at various NHLs.

TABLE X
PEL AND CLL FOR DIFFERENT HARDENING SCHEMES

NHL	CLL(MWh)	PELC ($\$10^6$)			OC ($\$10^6$)	HC ($\$10^6$)	TC ($\$10^6$)
		L_{VIT}	L_{IT}	L_G			
0	18 097	9.9	22.1	312.9	350.5	0.0	695.4
5	13 149	4.4	10.1	248.3	352.8	236.0	851.5
10	8891	2.3	5.7	172.3	354.9	400.0	935.3
15	6243	1.4	5.6	119.6	356.5	554.0	1037.1
20	4302	0.0	3.9	86.3	357.4	676.0	1123.6
25	3317	0.0	2.4	67.4	357.7	882.0	1309.6
30	1976	0.0	0.0	42.4	358.6	1024.0	1425.0
35	679	0.0	0.0	14.5	359.1	1201	1574.6

As indicated in Table X, the CLL and PELC in the hardening scheme show a trend of decreasing with increasing NHL. By contrast, the TC of the hardening scheme tends to increase. This occurs because larger systems exhibit greater resilience to disasters, leading to a lower initial load loss. Following this approach, as the HC experiences a pronounced increase, the reduction in the PELC is smaller than that in the HC. Consequently, the TC tends to increase.

The four scenarios presented in Table V are selected as examples, and these scenarios are denoted as follows: S1 (allowing 1026 MWh loss for L_{VIT}), S2 (allowing 2052 MWh loss for L_{IT}), S3 (allowing 7182 MWh loss for L_G), and S4 (allowing 1 0260 MWh loss for all loads). In accordance with the requirements of different scenarios, S1 includes a hardening scheme with NHL equaling 10 and a TC of 935.3 $\$10^6$, S2 includes a hardening scheme with NHL equaling 20 and a TC of 1123.6 $\$10^6$, while both S3 and S4 include a scheme with NHL equaling 35 and a TC of 1574.6 $\$10^6$. The scenario with differentiated load importance (S1) has superior economic value compared to the scenario without differentiated load importance (S4).

Furthermore, the value of the VLSP for the scenario with NHL equaling 10 is only 87.6%, necessitating the hardening of four additional lines to increase the index for this scenario to 100%. The TC of the scheme is 1021.3 $\$10^6$, reflecting an approximately 9.2% increase compared to that of the original scheme. For the same

NHL (NHL equals 14), the TC of C2 (scheme with two RAIs) is 1021.3 \$$10^6$. Compared with C1 (scheme with one RAI, LL), the VLSP of C2 increases by 93.6% to 100% at an additional cost of 16.4 \$$10^6$, or approximately 1.7%. Compared to C2, C1 is slightly more effective for reducing PELC, achieving an additional reduction of approximately 4.6 \$$10^6$, or approximately 3.3%. Additionally, incorporating one BESS at each of buses 3 and 10 results in a reduction in the total PEL from 83 065 MWh to 66 763 MWh, constituting an approximately 19.6% decrease.

V. Conclusion

This paper proposes a novel two-stage ROTEP model that incorporates the hardening of vulnerable lines under the impact of hurricanes. The proposed ROTEP model is validated using a modified IEEE RTS-24 and a two-area IEEE RTS-1996.

The simulation results indicate that: 1) recognizing the importance of loads during hurricane disasters and implementing a line hardening scheme for various classes of loads can significantly improve the economic efficiency of the scheme; 2) the proposed ROTEP model can be applied to increase the VLSP of a specified target, particularly for schemes with initially insufficient VLSP conditions; and 3) integrating additional BESSs during hurricane disasters effectively mitigates power energy loss, thereby enhancing the CLL.

This study has certain limitations. In this paper, the access locations for BESSs during disasters are autonomously defined, and future research can explore optimal BESS access locations through systematic planning methods. In future research, we aim to expand the dataset by including a greater number of hurricanes, on the basis of practical data, to increase the scheme's robustness for additional hurricane conditions[41]. Furthermore, we will study decomposition algorithms for MILP problems[42] to reduce the solution time of such problems and avoid potential convergence issues.

Appendix A

This section introduces the hurricane simulation process. The central pressure difference of hurricane $\Delta p(t)$ is expressed as:

$$\Delta p(t) = \Delta p_{\text{ini}} - 0.02(1+\sin\alpha)t \tag{A1}$$

where Δp_{ini} denotes the initial central pressure difference of the hurricane; and α is the angle between the hurricane motion direction and the coastline.

Then, the wind speed at a component location [43] $v_{\text{comp}}(t)$ can be calculated through (A2)–(A4):

$$v_g^{\max}(t) = k\sqrt{\Delta p(t)} \tag{A2}$$

$$v_{\text{H}}^{\max}(t) = 0.865 v_g^{\max}(t) + 0.5 v_{\text{H}}(t) \tag{A3}$$

$$v_{\text{comp}}(t) = \begin{cases} v_{\text{H}}^{\max}(t) \times d(t)/R_{\max}(t), & d(t) \leqslant R_{\max}(t) \\ v_{\text{H}}^{\max}(t) \times (R_{\max}(t)/d(t))^{0.6}, & d(t) > R_{\max}(t) \end{cases} \tag{A4}$$

where $v_g^{\max}(t)$ and $v_{\text{H}}^{\max}(t)$ denote the maximum gradient wind speed and wind speed at time t, respectively; K is a constant parameter, typically ranging from 6.93 to 6.97; $v_{\text{H}}(t)$ (m/s) denotes the translation speed of a hurricane at time t; $d(t)$ denotes the relative distance between components and the hurricane center at time t and can be obtained through (A5)–(A7):

$$d(t) = \sqrt{((x_{\text{comp}} - x(t)) + (y_{\text{comp}} - y(t)))} \tag{A5}$$

$$x(t) = x_{\text{ini}} + v(t)t\cos\alpha \tag{A6}$$

$$y(t) = y_{\text{ini}} + v(t)t\sin\alpha \tag{A7}$$

where $(x_{\text{comp}}, y_{\text{comp}})$ and $(x(t), y(t))$ denote the coordinates of the components and the hurricane center, respectively; $(x_{\text{ini}}, y_{\text{ini}})$ denotes the coordinates of the hurricane at landfall. The radius of the maximum wind speed $R_{\max}(t)$ of a hurricane is expressed as[44]:

$$\ln R_{\max}(t) = 3.859 - 7.7001\times10^{-5}\Delta p(t)^2 \tag{A8}$$

Appendix B

A transmission line failure model is introduced here. To consider the different wind speeds along long transmission lines, the lines are perceived as a sequence of interconnected line segments between adjacent towers. The failure probability of a transmission line is determined as the product of multiple line segments and towers.

A. Failure Rate of Line Segments and Towers

The failure rate of line segments and towers at different times based on a fragility model is given by [23]:

$$\mu_{m_k}(t) = \begin{cases} 0, & v_{mk}(t) \in [0, v_{\text{Tow}}^{\text{Des}}] \\ e^{0.2[v_{m_k}(t) - 2v_{\text{Tow}}^{\text{Des}}]}, & v_{mk}(t) \in (v_{\text{Tow}}^{\text{Des}}, 2v_{\text{Tow}}^{\text{Des}}) \\ 1, & v_{mk}(t) \in [2v_{\text{Tow}}^{\text{Des}}, \infty) \end{cases} \tag{B1}$$

$$\mu_{m_l}(t) = \exp[11 \times \frac{v_{m_l}(t)}{v_{\text{Line}}^{\text{Des}}} - 18]\Delta l \tag{B2}$$

where $\mu_{m_k}(t)$ and $\mu_{m_l}(t)$ denote the failure rates of the kth tower and lth line segment of the mth transmission corridor, respectively; $v_{m_k}(t)$ and $v_{m_l}(t)$ denote the wind speeds of the kth tower and lth line segment, respectively; $v_{\text{Tow}}^{\text{Des}}$ and $v_{\text{Line}}^{\text{Des}}$ denote the designed wind speeds of the kth tower and lth line segment, respectively; Δl is the length of each line segment, which is typically set to 350 m.

Based on the failure rate of each tower and line segment, the cumulative failure probability [23] of a line can be calculated through (B3)–(B4):

$$p_{m_k} = 1 - \exp\left\{-\sum_{i=0}^{N_K-1} \frac{\mu_{m_k}}{1-\mu_{m_k}}\Delta t\right\} \quad \text{(B3)}$$

$$p_{m_l} = 1 - \exp\left\{-\sum_{i=0}^{N_L-1} p_{m_l}(t)\Delta t\right\} \quad \text{(B4)}$$

Notably, all points on a line segment between two adjacent towers are assumed to be affected by the same wind speed.

B. Failure Model of a Transmission Corridor

The equivalent failure probability of a long transmission corridor, which is treated as a series of transmission towers connected to line segments, is formulated as:

$$P_m = 1 - \prod_{1}^{N_K}(1-p_{m_k})\prod_{1}^{N_L}(1-p_{m_l}) \quad \text{(B5)}$$

where N_K and N_L denote the total number of transmission towers and the total number of line segments in the mth transmission corridor, respectively.

APPENDIX C

The 24-hour fluctuations in the wind generation output and load values for the four typical scenarios are depicted in Figs. C1 and C2.

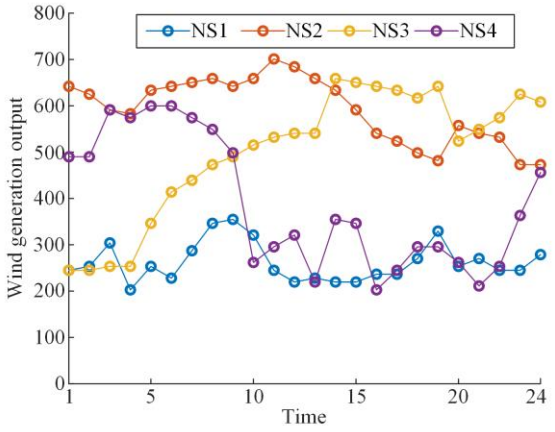

Fig. C1. 24-hour wind generation outputs for four typical scenarios.

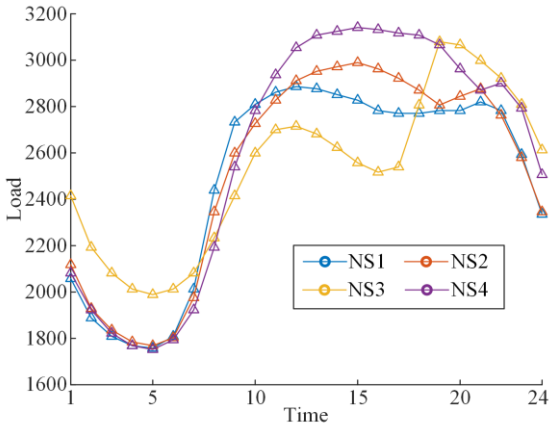

Fig. C2. 24-hour loads for four typical scenarios.

APPENDIX D

The geographic wiring diagram of the two-area IEEE RTS-1996 is shown in Fig. D1.

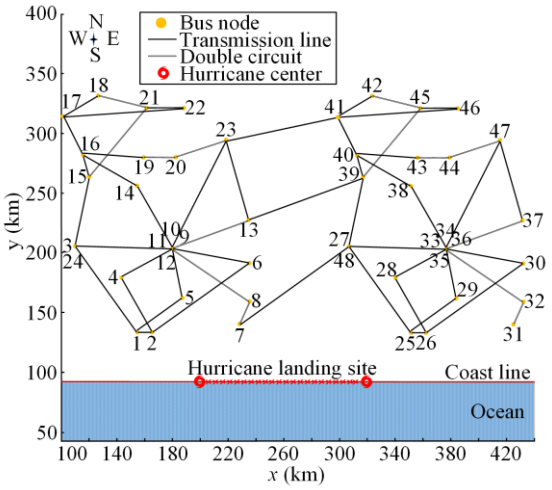

Fig. D1. Geographic wiring diagram of the two-area IEEE RTS-1996.

ACKNOWLEDGMENT

Not applicable.

AUTHORS' CONTRIBUTIONS

Jing Zhou: methodology, software, investigation, writing-original draft, writing-review & editing. Heng Zhang: validation and supervision. Haozhong Cheng: conceptualization and funding acquisition. Shenxi Zhang: writing-review & editing. Zheng Wang: formal analysis and software. Xiaohu Zhang: validation and visualization. All authors read and approved the final manuscript.

FUNDING

This work is supported by the National Natural Science Foundation of China (No. U23B6006 and No. 52307120).

AVAILABILITY OF DATA AND MATERIALS

Not applicable.

DECLARATIONS

Competing interests: The authors declare that they have no known competing financial interests or personal relationships that could have appeared to influence the work reported in this article.

AUTHORS' INFORMATION

Jing Zhou received the B.S. degree in electrical engineering from Southwest Jiaotong University, Sichuan, China, in 2017. He is currently pursuing the Ph.D. de-

gree in electrical engineering at Shanghai Jiao Tong University, Shanghai, China. His research interests include power system planning.

Heng Zhang received the Ph.D. degree in electrical engineering, Shanghai Jiao Tong University, Shanghai, China, in 2019. Now, he is an associate researcher in Shanghai Jiao Tong University. His main research interests are power market, and power system planning.

Haozhong Cheng received the Ph.D. degree in power systems from Shanghai Jiao Tong University, Shanghai, China, in 1998, respectively. He is current a professor in School of Electronic Information and Electrical Engineering, Shanghai Jiao Tong University. His research interests are mainly power system planning, operation, and deregulation.

Shenxi Zhang received the B.S. degree in electrical engineering from Hohai University, Nanjing, China, in 2011. He received the Ph.D. degree in electrical engineering from Shanghai Jiao Tong University, Shanghai, China, in 2016. He is currently an associate researcher with Shanghai Jiao Tong University. His main research interests include power system optimization, renewable generation, and integrated energy system.

Zheng Wang is a senior engineer of State Grid East China Branch. His research interests are mainly power system planning and operation.

Xiaohu Zhang is a senior engineer of State Grid East China Branch. His research interests are mainly power system planning.

REFERENCES

[1] A. B. Smith and R. W. Katz, "US billion-dollar weather and climate disasters: data sources, trends, accuracy and biases," *Natural Hazards*, vol. 67, no. 2, pp. 387-410, Feb. 2013.

[2] S. Frueh. (2014, Jul.), "Improving power system resilience in the 21st century resilient America roundtable," Jan. 2017[Online]. Available: http://sites.nationalacademies.org/ cs/ groups/pgasite/ documents/webpage/pga_153420.pdf

[3] Executive Office of the President (2013, Aug.). "Economic benefits of increasing electric grid resilience to weather outages," [Online]. Available: http://ieeexplore.ieee.org/xpl/articleDetails.jsp?arnumber=6978705

[4] Z. Bie, Y. Lin, and G. Li *et al*., "Battling the extreme: a study on the power system resilience," *Proceedings of the IEEE*, vol. 105, no. 7, pp. 1253-1266, Jul. 2017.

[5] J. Wu, J. Gu, and S. Liu, *et al*., "Strategies for improving resilience of regional integrated energy systems in the prevention resistance phase of integration," *Protection and Control of Modern Power Systems*, vol. 8, no. 2, pp. 1-17. Apr. 2023.

[6] C. Li, Y. Xi, and Y. Lu *et al*., "Resilient outage recovery of a distribution system: co-optimizing mobile power sources with network structure," *Protection and Control of Modern Power Systems*, vol. 7, no. 3, pp. 1-13, Jul. 2022.

[7] M. Panteli and P. Mancarella, "The grid: stronger, bigger, smarter?: presenting a conceptual framework of power system resilience," *IEEE Power and Energy Magazine*, vol. 13, no. 3, pp. 58-66, Apr. 2015.

[8] M. Mahzarnia, M. P. Moghaddam, and P. T. Baboli *et al*., "A review of the measures to enhance power systems resilience," *IEEE Systems Journal*, vol. 14, no. 3, pp. 4059-4070, Jan. 2020.

[9] A. Bagheri, C. Zhao, and F. Qiu *et al*., "Resilient transmission hardening planning in a high renewable penetration era," *IEEE Transactions on Power Systems*, vol. 34, no. 2, pp. 873-882, Mar. 2019.

[10] K. Jalilpoor, A. Oshnoei, and B. M. Ivatloo *et al*., "Network hardening and optimal placement of microgrids to improve transmission system resilience: a two-stage linear program," *Reliability Engineering & System Safety*, vol. 224, Aug. 2022.

[11] H. Wang, K. Hou, and J. Zhao *et al*., "Planning-oriented resilience assessment and enhancement of integrated electricity-gas system considering multi-type natural disasters," *Applied Energy*, vol. 315, Jun. 2022.

[12] M. Shivaie, M. Kiani-Moghaddam, and P. D. Weinsier, "Resilience-based tri-level framework for simultaneous transmission and substation expansion planning considering extreme weather-related events," *IET Generation, Transmission & Distribution*, vol. 14, pp. 3310-3321, May 2020.

[13] S. M. Moradi, T. Amraee, and S. S. Gougheri, "Deep learning based hurricane resilient coplanning of transmission lines, battery energy storages, and wind farms," *IEEE Transactions on Industrial Informatics*, vol. 18, no. 3, pp. 2120-2131, Apr. 2022.

[14] H. Ranjbar, S. Hosseini. and H. Zareipour, "Resiliency-oriented planning of transmission systems and distributed energy resources," *IEEE Transactions on Power Systems*, vol. 36, no. 5, pp. 4114-4125, Sept. 2021.

[15] Y. Yuan, H. Zhang, and H. Cheng *et al*., "Resilience-oriented transmission expansion planning with optimal transmission switching under typhoon weather," *CSEE Journal of Power and Energy Systems*, vol. 10, no. 1, pp. 129-138, Jan. 2024.

[16] B. Zhang, P. Dehghanian, and M. Kezunovic, "Optimal allocation of PV generation and battery storage for enhanced resilience," *IEEE Transactions on Smart Grid*, vol. 10, no. 1, pp. 535-545, Jan. 2019.

[17] T. Zhao, H. Zhang, and X. Liu *et al*., "Resilient unit commitment for day-ahead market considering probabilistic impacts of hurricanes," *IEEE Transactions on Power Systems*, vol. 36, no. 2, pp. 1082-1094, Mar. 2021.

[18] T. Ding, M. Qu, and Z. Wang *et al*., "Power system resilience enhancement in typhoons using a three-stage day-ahead unit commitment," *IEEE Transactions on Smart Grid*, vol. 12, no. 3, pp. 2153-2164, May 2021.

[19] H. Zhang S. Zhang, and F. Chen *et al*., "Enhancing power grid resilience against typhoon disasters by co-

ordinated scheduling of source-network-load," *IEEE Transactions on Industry Applications*, vol. 60, no. 1, pp. 1442-1453, Jan. 2024.

[20] Y. Rui and L. Yang, "Resilience assessment and improvement for electric power transmission systems against typhoon disasters: a data-model hybrid driven approach," *Energy Reports*, vol. 8, pp. 10923-10936, Nov. 2022.

[21] J. Yan, B. Hu, and K. Xie *et al*., "Data-driven transmission defense planning against extreme weather events," *IEEE Transactions on Smart Grid*, vol. 11, no.3, pp. 2257-2270, May 2020.

[22] M. Panteli, D. N.Trakas, and P. Mancarella, *et al*., "Power systems resilience assessment: hardening and smart operational enhancement strategies," *Proceedings of the IEEE*, vol. 105, no. 7, pp. 1202-1213, Jul. 2017.

[23] X. Liu, K. Hou, and H. Jia, "A planning-oriented resilience assessment framework for transmission systems under typhoon disasters," *IEEE Transactions on Smart Grid*, vol. 11, no. 6, pp. 5431-5441, Nov. 2020.

[24] X. Hamidpour, S. Pirouzi, and S. Safaee *et al*., "Multi-objective resilient-constrained generation and transmission expansion planning against natural disasters," *International Journal of Electrical Power & Energy Systems*, vol. 132, Nov. 2021.

[25] M. Panteli, D. N. Trakas, and P. Mancarella *et al*., "Boosting the power grid resilience to extreme weather events using defensive islanding," *IEEE Transactions on Smart Grid*, vol. 7, no. 6, pp. 2913-2922, Nov. 2016.

[26] E. Hossain, S. Roy, and N. Mohammad *et al*., "Metrics and enhancement strategies for grid resilience and reliability during natural disasters," *Applied Energy*, vol. 290, May 2021.

[27] A. Wang, Y. Luo, and G. Tu *et al*., "Vulnerability assessment scheme for power system transmission networks based on the fault chain theory," *IEEE Transactions on Power Systems*, vol. 26, no. 1, pp. 442-450, Feb. 2011.

[28] R. Rocchetta, E. Zio, and E. Patelli, "A power-flow emulator approach for resilience assessment of repairable power grids subject to weather-induced failures and data deficiency," *Applied Energy*, vol. 210, pp. 339-350, Jan. 2018.

[29] Y. Wang, C. Chen, and J. Wang *et al*., "Research on resilience of power systems under natural disasters-a review," *IEEE Transactions on Power Systems*, vol. 31, no. 2, pp. 1604-1613, Mar. 2016.

[30] M. Batts, L. Russell, and E. Simiu, "Hurricane wind speeds in the United States," *Journal of Structural Division*, vol. 106, no. 10, pp. 2001-2016, May 1980.

[31] J. Zhou, H. Zhang, and D. Liu *et al*., "Expansion planning method of transmission network considering cascading failures," *Electric Power Automation Equipment*, vol. 41, no. 12, pp. 136-142, Aug. 2021. (in Chinese)

[32] X. Wei, S. Gao, and T. Huang *et al*., "Complex network-based cascading faults graph for the analysis of transmission network vulnerability," *IEEE Transactions on Industrial Informatics*, vol. 15, no. 3, pp. 1265-1276, Mar. 2019.

[33] T. Wang, Y. Liu, and X. Gu *et al*., "Vulnerable lines identification of power grid based on cascading fault space-time graph," *Proceedings of the CSEE*, vol. 39, no. 20, pp. 5962-5972, Oct. 2019. (in Chinese)

[34] C. M. Mabel, E. R. Raj, and E. Fernandez, "Adequacy evaluation of wind power generation systems," *Energy*, vol. 35, no. 12, pp. 5217-5222, Dec. 2010.

[35] Probability Subcommittee. "IEEE reliability test system," *IEEE Transactions on Power Apparatus and Systems*, vol. 98, no. 6, pp. 2047-2054, Nov. 1979.

[36] C. Grig, P. Wong, and P. Albrecht *et al*., "The IEEE reliability test system-1996. A report prepared by the reliability test system task force of the application of probability methods subcommittee," *IEEE Transactions on Power Systems*, vol. 14, no. 3, pp. 1010-1020, Aug. 1999.

[37] Electrical and Computer Engineering Department, Illinois Institute of Technology. Index of data[EB/OL]. Available:http://motor.ece.iit.edu/data/6bus_Hourly_Data.xls

[38] H. Zhang, L. Cheng, and S. Yao *et al*., "Spatial-temporal reliability and damage assessment of transmission networks under hurricanes," *IEEE Transactions on Smart Grid*, vol. 11, no. 2, pp. 1044-1054, Mar. 2020.

[39] Central meteorological observatory database[EB/OL]. Available: http://typhoon.nmc.cn/web.html.

[40] Z. Yi, Z. Chen, and K. Yin *et al*., "Sensing as the key to the safety and sustainability of new energy storage devices," *Protection and Control of Modern Power Systems*, vol. 8, no. 2, pp. 1-22, Apr. 2023.

[41] R. Lu, X. Xiong, and H. Chen "Collaborative emergency defense strategy for offshore wind farm clusters considering the spatial-temporal characteristics of a typhoon," *Power System Protection and Control*, vol. 52, no. 12, pp. 13-24, Jun. 2024. (in Chinese)

[42] P. Li , H. Wan ,and X. Zhao *et al*., "A customized fix and implicate method for mixed integer linear programming models of unit commitment problems," *Power System Protection and Control*, vol. 51, no. 2, pp. 11-21, Jan. 2023.

[43] M. Chen, "The wind power reliability modeling research considering the effects of typhoon," M.S. thesis, Department of Power Systems and Automation., Guangxi University, Guangxi, China, 2014.

[44] P. J. Vickery, D. Wadhera and L. A. Twisdale *et al*., "U.S. hurricane wind speed risk and uncertainty," *Journal of Structural Engineering*, vol. 135, no. 3, pp. 301-320, Mar. 2009.